MICROSTRUCTURE PREDICTION IN A356 ALLOY CASTINGS

Q. Han and S. Viswanathan
Metals and Ceramic Division
Oak Ridge National Laboratory
P.O. Box 2008
Oak Ridge, TN 37831-6083

Abstract

As part of a program to develop advanced tooling for the design and optimization of structural A356 aluminum alloy castings, models have been used and developed for predicting microstructural length scales after solidification. The length scales are the primary dendrite size, secondary dendrite arm spacing and cell spacing for the primary aluminum phase and the particle/rod length, diameter and spacing for the silicon phase. Mechanisms governing the growth of these phases are considered in the models. The predictions are compared with independent measurements by other researchers and with data from the literature. A good fit with experimental data is obtained. The results of the models are presented in the form of analytical equations for each of the length scales. The simple form of the equations allows them to be used in the postprocessing step of commercial solidification codes for the prediction of microstructure in shape castings.

Introduction

The mechanical properties of cast aluminum alloys are largely dependent upon the solidification microstructure of the alloys. The service life of a cast component is determined by the microstructural distribution throughout the casting, especially in those regions that are critically stressed. In the drive toward lightweight vehicle production, the description and prediction of the microstructure in shape castings has become important. This is because the microstructure length scales are required in the mechanical property models used for design optimization. The use of predictive property models are critical due to the need to replace heavy ferrous parts with aluminum alloy castings and the limited experience with the use and long term performance of aluminum alloy castings. This paper focuses on the description and prediction of the solidification microstructure in A356 aluminum alloys (Al, 8 wt % Si, 0.4 wt % Mg) used in structural automotive and aerospace components.

The development of the solidification microstructure in A356 aluminum alloys is well documented in the literature (1). On cooling, aluminum-rich dendrites first precipitate from the melt. A eutectic constituent, comprising of aluminum-rich and silicon phases, then grows between the aluminum-rich dendritic network. The morphology of the silicon phase is either rod-like or plate-like depending on whether the melt has been treated with modifiers such as sodium or strontium. On a two dimensional metallographic section, the silicon rods look like particles and the silicon plates look like rods. To describe the morphology of the primary aluminum-rich phase, we need the primary dendrite spacing, d_1, secondary dendrite arm spacing, d_2, and cell spacing, d_C. The cell spacing is defined as the average length intersecting dendrites using random lines. d_C is a useful parameter as it can be conveniently measured by image analysis techniques. To describe the morphology of the silicon phase, we need parameters such as the silicon rod/particle diameter, a, silicon spacing, λ, and silicon rod length, l.

In this paper, each of these length scales is discussed in detail. Analytical equations are generated for these length scales that can be incorporated in commercial software for the prediction of microstructure in shape castings.

Prediction of Primary Dendrite Spacing

The primary dendrite model for A356 alloy developed in this study is based on a recently successful model reported by Hunt and Lu (2-3) for dendrite array growth in binary alloys. Although the model describes the physics of dendritic array growth under directional solidification conditions, it is likely that the prediction can be extended to treat primary dendrite size during equiaxed grain growth. This is because in the case of equiaxed grains, the competitive growth of the dendrites at the liquidus isotherm is identical to that during directional solidification. Details of the primary dendrite model for A356 alloys have been presented elsewhere (4).

Comparison of the primary dendrite model's predictions with data from the literature for Al-Si-Mg alloys is shown in Figure 1. The solid line in Figure 1 is the minimum stable spacing predicted by the model and the dashed line is the maximum spacing taken as three times the minimum spacing (5). The titled squares are the experimentally measured average spacing taken from the data in the literature (6). As expected, the measured average spacing falls into a band defined by the calculated minimum stable spacing and the maximum stable spacing for the silicon concentration varying from 0.3 to 5 at. % and the magnesium concentration varying from 0.14 to 2.25 at. %.

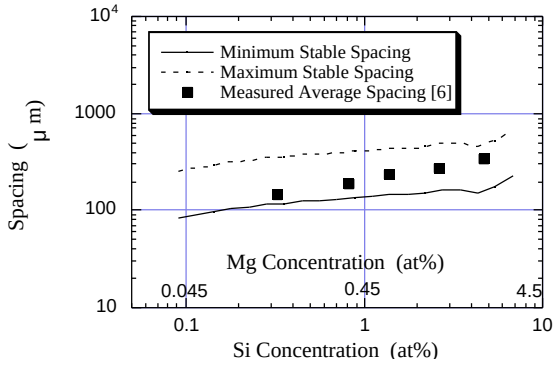

Figure 1: A comparison of calculated and experimental results for primary dendrite spacing for Al-Si-Mg alloys (4).

Comparison of the model's prediction with experimental measurements on transparent materials (3,7) is shown in Figure 2. Dendrite overgrowth was observed for conditions represented by the open circles. The resulting spacing is smaller than the calculated minimum stable spacing represented by the solid line. Tertiary arms were observed to grow into primary dendrites for conditions represented by the open triangles. The resulting spacing appears to be close to the maximum stable spacing. An interesting result is that the average spacing (represented by the filled circles and triangles in Figure 6) appears to depend on the history of the specimen. If the growth velocity, *V*, decreased in steps during the experiment, the resulting average spacing is almost equal to the predicted minimum stable spacing. This observation indicates that, in a casting, the average primary dendrite spacing is likely to be the minimum stable spacing, since the growth velocity of the solid decreases from the surface to the center of a casting.

Analytical Expressions for Primary Dendrite Spacing

Having validated the model's predictions, the model can be used to predict primary dendrite spacings under various casting conditions for A356 alloys. Data used in the calculation for A356 alloys are listed in the nomenclature section. Figure 3 shows the calculated primary dendrite spacing at various temperature gradients and growth velocities covering a large range of casting conditions. Figure 3 represents a family of primary dendrite spacing versus growth velocity curves obtained by varying the temperature gradient at the dendrite tips. One characteristic of these curves is that one curve can be reproduced by another by simply translating the second curve. This suggests that all the curves can be compressed into one. Multiplying the d_1 value by $(G/G_0)^{0.63}$ and the V value by $(G/G_0)^{-0.67}$ for each point in each curve, where G_0 is taken as 10000 K/m, we obtain a single curve in Figure 4 for all the data in Figure 3. As indicated in the literature, the minimum stable spacing is governed by the interaction of the neighboring dendrites at low growth rates and by the Peclet number at high growth rates (3,5). Consequently, it is better to fit the curve in Figure 4 using two functions.

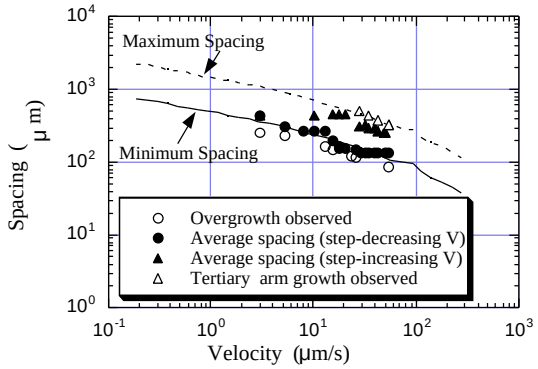

Figure 2: A comparison of the predicted and the experimental primary spacing for succinonitrile ethanol alloys. The predicted minimum and maximum stable spacings are represented by the solid and the dashed line, respectively (3).

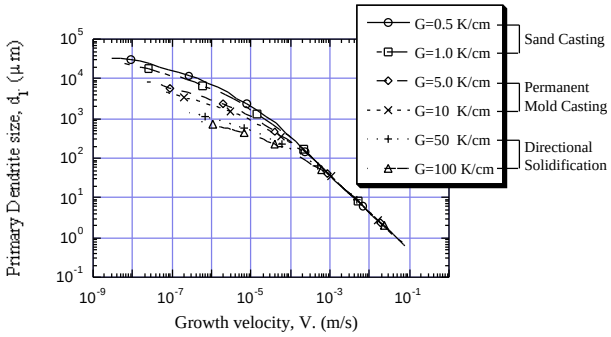

Figure 3: Relationship between the primary dendrite arm spacing and growth velocity for a range of casting conditions.

For $V(G/G_0)^{-0.67}<10^{-3}$, the equation that best fits the data is

$$d_1 = 70.73V^{-0.42}G^{-0.35} \quad , \tag{1}$$

while for $V(G/G_0)^{-0.67} >10^{-3}$, d_1 is only a function of V and is given by

$$d_1 = 0.0576V^{-0.94} \quad . \tag{2}$$

Equations 1 and 2 can be used to predict the primary dendrite size in A356 alloys for most casting conditions.

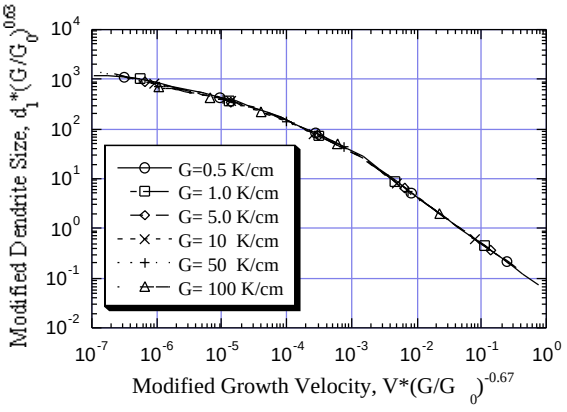

Figure 4: A single curve generated for all the data in Figure 3 by a mathematical transformation.

Secondary Dendrite Arm Spacing

Mathematical models have been developed for describing the isothermal coarsening of secondary dendrite arm spacing in binary alloys based on the geometric models shown in Figure 5, (refs. 8-10). These models have been recently extended to treat multi-component alloys (11) such as A356. For alloys in which the interaction between the solute elements is small, a relationship between the local solidification time and secondary dendrite arm spacing is proposed to be

$$t_C = \frac{Ld_2^3}{\sigma T_0}\phi \sum_{i=1}^{N} \frac{m_i C_{ri}(1-k_i)}{D_{ii}} \quad , \tag{3}$$

where ϕ is a constant depending on the geometric model used and C_{ri} is estimated using the Scheil equation:

$$C_{ri} = C_{0i}(1-g_S)^{(k_i-1)} \quad . \tag{4}$$

For binary alloys, N=1 and Eq. 3 reduces to the well-known equations given in the literature (8-10). Also, for this case, g_s = 0.5, to allow the isothermal coarsening model to be used to estimate the final secondary dendrite arm spacing after solidification (8).

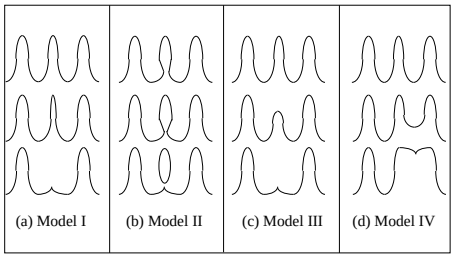

Figure 5: Geometric models for dendrite coarsening: (*a*) radial remelt model, Model I, (*b*) neck remelt model, Model II, (*c*) axial model, Model III, and (*d*) coalescence model, Model IV.

Comparison of the secondary dendrite arm spacing prediction using Eq. 3 and experimental measurements in the literature (12) is given in Figure 6. All the four geometric models predict the right trend of the dependence of d_2 on composition. This suggests that the relationship between the secondary dendrite arm spacing and composition can be described using Equation 3 for these alloys. Model II seems to fit the measurements better than Models I, III, and IV. Since Eq. 3 is derived considering diffusion only but experiments were carried out under conditions under which fluid flow in the liquid is inevitable, it is likely that Model II predominates in the presence of fluid flow. However, since all four models have been observed in experiments, one cannot claim that Model II represents the primary mechanism for secondary dendrite arm coarsening. For the purpose of this effort, however, the value of ϕ=0.00852 corresponding to that of Model II is suggested for the prediction of d_2 under casting conditions.

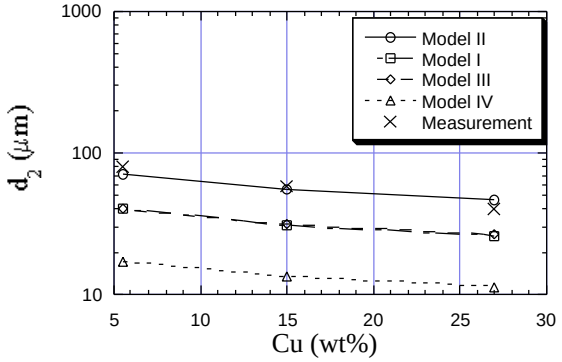

(*a*)

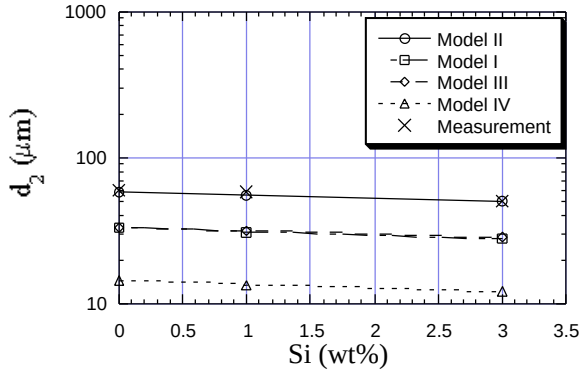

(*b*)

Figure 6: A comparison of theory with experiment for secondary dendrite arm spacings in Al-Cu-Si alloys: (*a*) Al-1% Si-X% Cu, and (*b*) Al-1.5% Cu-X% Si.

Equation 5 is obtained by using Eq. 3 for Al-Si-Mg ternary alloys corresponding to the composition of A356. These equations can be used to calculate the secondary dendrite arm spacing as a function of the local solidification time and composition in A356 alloys.

$$t_C = -d_2^3 \frac{L}{\sigma T_0}\left(\frac{m_{Si}C_{Si}(1-k_{Si})(1-g_s)^{(k_{Si}-1)}}{D_{Si}} + \frac{m_{Mg}C_{Mg}(1-k_{Mg})(1-g_S)^{(k_{Mg}-1)}}{D_{Mg}}\right) \quad . \quad (5)$$

Dendrite Cell Spacing

The cell spacing, which is the average intercept of a random line intersecting dendrites, is a useful parameter for image analysis. This is because in many cases the primary dendrite size and the secondary dendrite arm spacing are not easily measured. As illustrated in Figure 7, the basic microstructural feature for the aluminum-rich primary phase consists of randomly distributed secondary arms. The length of a secondary arm is approximately $d_1/2$ and the diameter is approximately d_2. Since a random line intersecting secondary arms is likely to produce an intercept length that falls between $d_1/2$ and d_2, one should be able to estimate the cell spacing using

$$d_C = \frac{(d_1/2 + d_2)}{2} \quad . \quad (6)$$

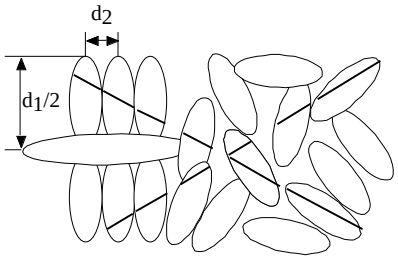

Figure 7: Schematic diagram showing the length scales needed to describe the morphology of aluminum-rich dendrites.

Silicon Rod Length

Little information is available on the prediction of silicon rod length. Experimentally, it has been shown that the eutectic nucleates and grows on the primary aluminum phase (1). Figure 8 illustrates this growth morphology for an Al-11 wt % Si alloy. In the lower part of Figure 8, we can see a primary aluminum dendrite surrounded by radiating silicon needles. A similar growth pattern may be expected for the eutectic silicon in A356 alloy, although it is less evident in a metallographic specimen due to the lower silicon content (7.0%) in the alloy. The reason the eutectic silicon nucleates on the primary aluminum phase is that silicon is rejected by the growing dendrites and is most enriched at the dendrite surface. Also, while the volume fraction of primary aluminum phase in an Al-11% Si alloy would be small, the volume fraction of primary aluminum phase in A356 alloy is about 52%, producing a coherent contiguous network. This allows us to construct a representative volume element around each primary aluminum dendrite that contains a distribution of phases that is representative of the overall microstructure. Such a representative volume construction is illustrated in Figure 9 where the black phase is the silicon phase that branches by a twinning mechanism (13). The average length of silicon rods is defined by *l*. Knowing the volume fractions of the primary dendrite phase and the eutectic, the average length of the silicon rods can be related to the primary dendrite size based on simple geometric considerations.

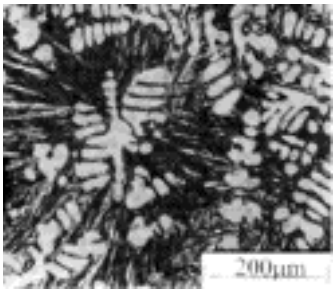

Figure 8: Microstructure showing that the eutectic grows from a dendrite in an Al-11wt % Si alloy (1).

In Figure 9, the volume fraction of the primary aluminum phase is given by

$$1 - g_E = \frac{\pi(d_1/2 - l)^2}{\pi(d_1/2)^2} \quad . \quad (7)$$

Rearrangement of Eq. 7 yields

$$l = \frac{d_1}{2}(1 - \sqrt{1 - g_E}) \quad . \quad (8)$$

In Eq. 8, g_E can be calculated using thermodynamic software such as ThermoCalc™ and d_1 is given by Eqs. 1 and 2. The average length of silicon rod is thus a function of g_E and d_1.

Silicon Rod/Particle Diameter

The microstructure observed in the transverse section perpendicular to the growth direction of the silicon phase is illustrated in Figure 10, in which a is the silicon rod diameter and λ is the silicon rod spacing. Once again simple geometric considerations can be used to relate these two parameters resulting in the following equation:

$$g_{Si} = \frac{\pi a^2/4}{\pi\lambda^2/4} \quad , \quad (9)$$

where g_{Si} is the silicon volume fraction in the eutectic and can be calculated using ThermoCalc™. For A356, g_{Si} equals 0.14. Rearrangement of Eq. 9 gives

$$a = \lambda\sqrt{g_{Si}} \quad . \quad (10)$$

Extensive studies have been carried out to determine the growth law for eutectics and to obtain the spacing, λ (14-19). For a nonfaceted interface, the most successful theory is that of Jackson and Hunt (14) that proposes the following growth law correlating the eutectic spacing, λ, with the growth velocity of the solid, V_S:

$$\lambda^b V_S = c \quad , \quad (11)$$

where *b* and *c* are constants. Efforts have been made to extend the Jackson-Hunt model to treat nonfaceted/faceted eutectic

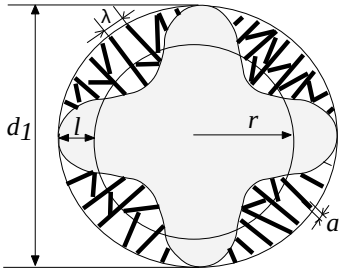

Figure 9: Schematic diagram showing the relationship between the primary dendrite size and the average length of the silicon phase.

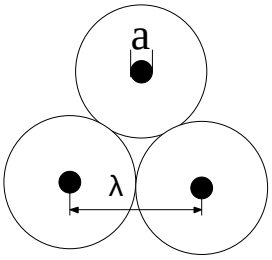

Figure 10: Schematic diagram illustrating the relationship between the spacing and diameter of silicon.

systems (16-17) but several nonphysical assumptions have been made. Experimental approaches to validate the growth law for non-faceted systems have also been carried out and it has been found that the constants *b* and *c* vary with alloy and temperature gradient (8-19). For modified Al-Si binary alloys, the growth law is in the form (18)

$$\lambda = 0.0311 V_S^{-0.446} \quad . \tag{12}$$

No tests of this growth law for A356 alloy are available in the literature. Based on experimental data generated (20) in connection with this program, the following form of the growth law is proposed for the silicon spacing

$$\lambda = 0.16 V_S^{-0.446} \quad , \tag{13}$$

Validation of the Models on Plate Casting

The analytical equations given in the above sections were used in the postprocessing step of a commercial solidification package, ProCAST™, for the prediction of microstructural length scales in a plate casting. The predictions were then compared with independent experimental measurements (20) on plate castings of A356 alloy (7 wt % Si, 0.4 wt % Mg). Plate castings of dimensions 229 × 140 × 38 mm were cast in sand molds with cast iron chills on the top, bottom, and end of the plate. The sides of the plate were left unchilled. Measurements were taken along the vertical center plane of the casting. The length scales compared in this section are cell spacing, silicon length and silicon diameter.

The comparison of predicted dendrite cell spacings with experimental measurements is shown in Figure 11. The cell spacing was calculated using Eq. 6. Very good agreement between the prediction and the measurements is evident.

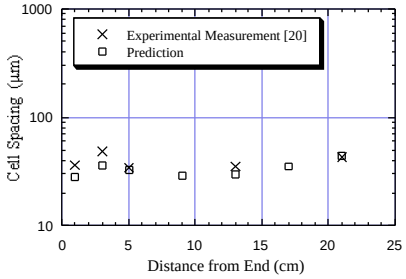

Figure 11: Comparison of the model's predictions with experimental measurements of dendrite cell spacing for A356 alloy cell spacing.

Figure 12 shows the comparison of the predicted silicon rod length and experimental measurements. Once again, the predictions fit well with experimental data. Considering that Eq. 8 is semi-quantitative in nature, the comparison shown in Figure 12 is better than expected.

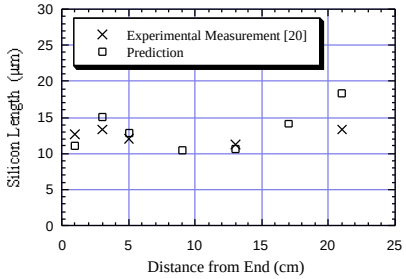

Figure 12: Comparison of the model's predictions with experimental measurements of silicon rod length for A356 alloy.

Figure 13 shows a comparison of the predicted silicon rod diameter with data from experimental measurements. The use of the growth law in the form of Eq. 11 gives a silicon rod size a half an order of magnitude smaller than the measurements. A good fit with experimental data is obtained using the modified constant in Eq. 12. However, Eq. 12 must be considered to be strictly empirical. Clearly, fundamental research is needed to determine the growth law for eutectic formation with a faceted solid-liquid interface.

Conclusions

Models have been developed for the prediction of microstructural length scales in A356 aluminum alloys. These length scales are the primary dendrite spacing/size, secondary dendrite spacing, dendrite cell spacing and silicon rod length, size and spacing. Analytical equations have been derived that can be easily incorporated in the post processing step of commercial solidification codes. Comparison of predictions of microstructural

length scales using these analytical equations with experimental measurements shows excellent agreement. Accordingly, the models described in this paper provide a convenient and viable approach for determining the microstructural length scales in A356 aluminum alloy casting that are needed in mechanical property and component life prediction models.

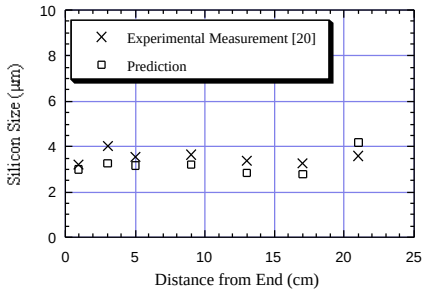

Figure 13: Comparison of the predictions using a modified growth law constant with experimentally measured silicon rod diameter/size.

Acknowledgments

The authors thank John Vitek and Ted Huxford for reviewing the paper and Millie Atchley for preparing the manuscript.

This work was performed under a Cooperative Research and Development Agreement (CRADA) with the United States Advanced Materials Partnership (USAMP), United States Council for Automotive Research (USCAR) for the project on Design and Product Optimization for Cast Light Metals. This research was sponsored by the U.S. Department of Energy, Assistant Secretary for Energy Efficiency and Renewable Energy, Office of Transportation Technologies, Lightweight Vehicle Materials Program, under contract DE-AC05-96OR22464 with Lockheed Martin Energy Research Corp. This research was supported in part by appointments to the Oak Ridge National Laboratory Postdoctoral Research Associates Program, administered jointly by the Oak Ridge Institute for Science and Education and the Oak Ridge National Laboratory.

Nomenclature

a	diameter of silicon particles, size of secondary dendrite arm	
C_{0i}	bulk composition of the *i*th element	wt%
C_{ri}	the *i*th element composition near the secondary arm of size *r*	wt%
C_{Si}	bulk silicon composition	wt%
C_{Mg}	bulk magnesium composition	wt%
d_1	primary dendrite arm spacing	μm
d_2	secondary dendrite arm spacing	
d_C	dendrite cell spacing	
D_{ii}	diffusion coefficient of the *i*th element	
D_{Si}	diffusion coefficient of Si in the liquid	3.3×10^{-9}m^2/s (4)
D_{Mg}	diffusion coefficient of Mg in the liquid	3.3×10^{-9}m^2/s (4)
G	temperature gradient	K/m
g_S	solid volume fraction	0.52 in A356
g_E	eutectic volume fraction	0.48 in A356
g_{Si}	silicon volume fraction in the eutectic	0.14 in A356
k_i	solute distribution coefficient of the *i*th element	
k_{Si}	Si solute distribution coefficient	0.110 (4)
k_{Mg}	Mg solute distribution coefficient	0.177 (4)
m_i	equilibrium liquid slope for the *i*th element	
m_{Si}	equilibrium liquidus slope for Si	-6.61 K/wt% (4)
m_{Mg}	equilibrium liquidus slope for Mg	-2.89 K/wt% (4)
N	number of solute elements in a multicomponent alloy	
l	length of silicon particles	
L	latent heat of the primary aluminum phase	1.05×10^9 J/m^3 (8)
t_c	local solidification time	s
T_0	liquidus temperature; for A356 aluminum alloy, T_0 = 889K	
V	local growth velocity	m/s
V_S	velocity of the solidus (eutectic isotherm)	m/s
σ	interface free energy	5.02×10^{-2} J/m^2 (8)
ϕ	constant of the coarsening models	8.52×10^{-3} (Model II)
λ	eutectic phase spacing, silicon spacing in A356	μm

References

1. L. Bäckerud, G. Chai and J. Tamminen: "Solidification Characteristics of Aluminum Alloys", Vol.2: Foundry Alloys, AFS/SKANALUMINUM, 1990.
2. Shu-Zu Lu and J.D. Hunt: J. Cryst. Growth, 123 (1992), pp. 17-34.
3. J.D. Hunt and Shu-Zu Lu: Metall. Trans, 27A (1996) 611.
4. Q. Han and J.D. Hunt: Mater. Sci. Eng., A238 (1997), pp.192-95.
5. X. Wan, Q. Han and J.D. Hunt: Acta Mater., 45 (1997), pp. 3975-79.
6. D.G. McCartney and J.D. Hunt: Acta. Metall., 29 (1981), pp. 1851-63.
7. W. Huang, X. Geng and Y. Zhou: J. Cryst. Growth, 134 (1993), pp. 105-115.
8. T.Z. Kattamis, J.C. Coughlin and M.C. Flemings: Trans. AIME, 239 (1967) 1504-11.
9. J.J. Reeves and T.Z. Kattamis: Scripta Metall., 5 (1971), pp.223-29.
10. Kuang-Ho Chen and T.Z. Kattamis: Z. Metallkd., 61 (1970), pp. 475-79.
11. Q. Han, H, Hu and X. Zhong: Metall. Mater. Trans., 28B (1997), pp. 1185-87.
12. J.E. Mori, K. Ogi and K. Matsuda: J. Jpn Inst. Met., 40 (1976), pp. 406-11.
13. S.Z. Lu and A. Hellawell: Metall. Trans., 18A (1987), pp. 1721-1733.
14. K.A. Jackson and J.D. Hunt: Trans. Am. Inst. Min. Engrs, 236 (1966), p. 1129.
15. R. Trivedi, P. Magnin and W. Kurz: Acta. Metall., 35 (1987), pp. 971-980.
16. T. Sato and Y. Sayama: J. Crystal Growth, 22 (1974), p.259.
17. P. Magnin and W. Kurz: Acta. Metall., 35 (1987), pp. 1119-1128.
18. L.M. Hogan and H. Song, Metall. Trans., 18A (1987), p. 707.
19. B. Toloui and A. Hellawell: Acta Metall., 24 (1976), p.565.
20. A.M. Gokhale, unpublished report and private communication, 1999.